Proc. 2001 AVS Int. Symp. Liquid Metal Processing and Casting, Santa Fe, 2001. Eds. A.Mitchell, J.V-D.Avyle

MODELLING THE DYNAMICS OF ELECTROMAGNETICALLY AGITATED METALLURGICAL FLOWS: LEVITATION, COLD CRUCIBLE, ALUMINIUM ELECTROLYSIS, ETC.

V.Bojarevics[1], K.Pericleous[1] and J.Freibergs[2]

[1] *University of Greenwich, CMS, 30 Park Row, SE10 9LS, London, UK*
[2] *Institute of Physics, Salaspils-1, Latvia*

E-mail: V.Bojarevics@gre.ac.uk

Abstract. We present practical modelling techniques for electromagnetically agitated liquid metal flows involving dynamic change of the fluid volume and shape during melting and the free surface oscillation. Typically the electromagnetic field is strongly coupled to the free surface dynamics and the heat-mass transfer. Accurate pseudo-spectral code and the k-omega turbulence model modified for complex and transitional flows with free surfaces are used for these simulations. The considered examples include magnetic suspension melting, induction scull remelting (cold crucible), levitation and aluminium electrolysis cells. The process control and the energy savings issues are analysed.

Introduction

Electromagnetically driven turbulent flows occur in a large variety of industrial applications like continuous casting, vacuum arc remelting, electroslag remelting, liquid metal treatment stirring and transport, aluminium electrolysis, induction melting, magnetically stabilised crystal growth and many others [9]. Electromagnetic processing of liquid metals quite often involves dynamic change of the fluid volume interfacing with a melting solid material, gas or vacuum, and possibly a different liquid. Typically the flow is turbulent, the characteristic velocity being of the order 0.1 – 1 m/s. The electromagnetic field and the associated force field are strongly coupled to the free surface dynamics and the heat-mass transfer. We present here a review of our work done for practical modelling of the flow and heat transfer using the accurate pseudo-spectral code and the k-omega turbulence model suitable for complex and transitional flows with free surfaces. The electromagnetic field is modelled by the integral equation based finite element method.

One of the most typical cases, the melting liquid metal flow in an induction furnace, is the subject of numerous attempts of simulation both experimentally and numerically, see References [1-6], to mention but a few. Experiments [1-5] show that the liquid metal flows are highly turbulent and subject to large scale time-dependent fluctuations. The turbulent mixing controls the distribution of the produced thermal energy into the melt and therefore has to be correctly simulated. Induction melting is an ideal method for the processing of reactive metals,

such as titanium aluminides (Ti-Al), since contact with the crucible wall can be kept to a minimum by the electromagnetic confinement. However, success of the process and its widespread use depends critically on improving its energy efficiency. The goal of the numerical simulation is to identify the heat losses in the coil, crucible and metal, and devise ways of improving thermal efficiency.

The AC electromagnetic field skin layer depth is of considerable extent in most practical cases of induction melting and liquid metal treatment, typically 10-20% of the fluid region radius. The high frequency approximation where the electromagnetic force distribution can be effectively replaced by modified boundary conditions [6] is not really applicable. In the present work we are using the full electromagnetic force representation and the exact dynamic stress boundary conditions. The solution is found by the pseudo-spectral code recently developed for a similar problem of the semi-levitation melting [8], which is supplemented by the k-ω turbulence model [7]. According to this approach, the computation follows in detail the time development of the turbulent characteristics and the time dependent flow field. The validation of this modelling was presented in [5] for the case of detailed experimental measurements within the liquid metal (In-Ga-Sn) at room temperature.

As examples for the AC melting industrial applications we will consider the magnetic induction suspension and cold crucible dynamic simulations accounting for the melting front motion and the free surface changes. The magnetic induction cold crucible technique is used to melt high temperature reactive metals (like titanium alloys) without direct contact to a crucible wall. Ideally the crucible bottom wall would be protected by a thin layer of solidified metal and by magnetically confining the liquid metal some distance away from the side wall at all stages of the melting process. In the suspension melting the crucible sidewalls are absent and the molten metal is confined solely by the AC magnetic field from the dynamically moving coil at the speed matching the melting front progress. The melting process takes a considerable time and power, and it is essentially dynamic.

In the extreme case of complete magnetic levitation it is possible to melt, stir and shape pure or reactive metals without any contact to crucible walls. The levitation confinement permits also uncontaminated metallurgical experiments to be conducted, to measure physical properties of liquid metals, e.g., to measure surface tension, observe the nucleation and the solidification process, determine the existence of magnetic ordering. However, the magnetically levitated molten metal is subject to complex fluid dynamics interaction between the internal fluid motion and the free surface shape. In addition, the electromagnetic force distribution is affected both by the free surface shape and by the position of the liquid volume relative to the magnetic field generating coil. Different local and global instabilities can result because of this complex interaction.

The pioneering work by Okress et al. [10] showed the difficulty to achieve stable levitation and the melt confinement in experiments even for small specimens of about 1-2 cm dimensions. Numerous experimental and theoretical investigations were attempted to achieve better understanding of the basic physical mechanisms controlling the levitation dynamics, [11-16]. Theoretical and numerical methods developed to describe the AC high frequency (typically of the order 10^4-10^5 Hz) electromagnetic field were based on the assumption of an infinitesimal penetration depth for the magnetic field and the induced electric current. The electromagnetic force is then confined to the skin layer depth at the external boundary of the liquid metal. This assumption effectively ignores the force distribution within the finite size real skin layer and accounts for the electromagnetic effects in the boundary conditions only. There is now growing evidence, showing that this approximation is not always applicable in the case of the moderately high frequencies used in practical applications ([13,17] and references therein). The thin *skin-layer* approximation is violated also because of the highly curved liquid metal shape and the non-uniformity of the magnetic field. In this paper we will

present numerical solutions for the full fluid dynamic problem by using the spectral solution technique. The only restriction is the axial symmetry of the problem. The time dependent co-ordinate transformation will be used to track the free surface position where the exact dynamic stress boundary conditions are satisfied. When the gravity is present, the resulting velocity fields are turbulent even for a typical melt volume size of order 0.01 m. We demonstrate the oscillating behaviour of the free surface, centre of mass, and the total electromagnetic force acting on the levitated fluid volume. In the case of an idealised pure experiment comparisons will be made for the solutions with the full electromagnetic force included and the solution obtained replacing the body force by the effective magnetic pressure modification of the boundary conditions (the usual approach used to obtain the free surface shape). The physical reason for the fundamental discrepancy found for these solutions is the difference in the electromagnetic force representation: only the gradient part of the full force is accounted for in the "magnetic pressure" approximation.

The similar ideology spectral modelling is applied to an industrial electrolysis cell, used to produce primary aluminium, which can sustain highly coupled non-linear waves at the interface of the liquid aluminium and the electrolyte layers where a turbulent flow takes place. The penetrating electric current and the associated magnetic field are intricately involved in the oscillation process, and the observed wave frequencies are shifted from the purely hydrodynamic ones [22]. The wave development depends on the magnetic field distribution created by the whole network of current supplying busbars and the current within the cell. Numerical simulation of aluminium electrolytic reduction process is the much-appreciated support for today's high amperage smelter technology design and cell retrofit. Aluminium electrolysis is a complex process involving different physical and chemical phenomena often interacting with each other. Cell optimisation is based on numerical simulation of MHD processes in the cell's liquid metal and electrolyte zone. The optimisation implies simulation and comparison of cell models with different configurations of current supplying busses, ferromagnetic materials or other cell parameters. Accurate calculation of the final, top level cell effectiveness criteria, such as current efficiency, specific energy consumption, interface and thermal stability, material costs or operational and environmental safety, needs full representation of cell's physical and chemical processes and is extremely complicated [18]. The present paper contains a generalisation of the previous weakly non-linear wave equations [19, 20] by accounting for the turbulent horizontal circulation flows in the two fluid layers. The electromagnetic simulation is extended to include not only the fluid layers, but also the whole bus bar circuit and the ferromagnetic construction parts effects. A comparison for the linear and the non-linear waves will be demonstrated. A realistic industrial cell configuration, including a ledge at the cell bottom, individual anodes and cathode bars, and electrolyte channels, is used for the wave and flow dynamic simulations.

Modelling Principles

The present modelling approach is based on the turbulent momentum and heat transfer equations:

$$\begin{aligned} &\partial_t \mathbf{v} - \mathbf{v}\times(\nabla\times\mathbf{v}) = -\nabla(\rho^{-1}p + \tfrac{1}{2}|\mathbf{v}|^2) + \nabla\cdot(\nu_e(\nabla\mathbf{v} + \nabla\mathbf{v}^T)) - K_D\mathbf{v} + \rho^{-1}\mathbf{f} + \mathbf{g}, \\ &C_p^*(\partial_t T + \mathbf{v}\cdot\nabla T) = \nabla\cdot(C_p\alpha_e\nabla T) + \rho^{-1}|\mathbf{J}|^2/\sigma, \\ &\nabla\cdot\mathbf{v} = 0, \end{aligned} \tag{1}$$

where **v** is the velocity vector, p - the pressure, ρ - the density, ν_e is the effective turbulent viscosity, $-K_D\,\mathbf{v}$ is a Darcy term representing the mushy zone and the melting front modelling, **f=J×B** is the electromagnetic force, g - the gravity, T - the temperature, α_e - the effective turbulent thermal diffusivity, C_p - the specific heat, C_p^* - the solid fraction modified specific heat function which accounts for latent heat effects (see [8] for details), and J^2/σ is the Joule heat. The boundary conditions used for the fluid flow problem are: the no-slip condition for the velocity at solid walls:

$$\mathbf{v} = 0\ ; \tag{2a}$$

at the free surface normal stress is compensated by the surface tension only, tangential stress is zero, and the kinematic condition states that the new interface location moves with material fluid particles:

$$\Pi_{nn} = \gamma K\ ;\quad \Pi_{n\tau} = 0\ ;\quad \mathbf{e_n}\cdot\partial_t\mathbf{R} = \mathbf{e_n}\cdot\mathbf{v}\ , \tag{2b}$$

where Π is stress tensor, e_n and $\mathbf{e}_\tau$ - normal and tangent unit vectors at the free surface, γ -the surface tension coefficient, K - the local mean curvature of the surface, R - the position vector of the interface. For the temperature boundary conditions we adopt the radiation and the effective heat transfer at solid walls. The respective expressions in co-ordinate representation are given in [8]. The temperature boundary conditions depend on the local turbulent thermal diffusion coefficient α_e, which is proportional to the effective turbulent viscosity ν_e determined from the numerical k-ω turbulence model [7]. The k-ω model used is a low Re number version which resolves the flow from laminar to developed turbulent states, and therefore is considered suitable for turbulent flow evolution simulations. The effective viscosity is the sum of laminar and turbulent viscosity, $\nu_e(r,z,t) = \nu + \nu_T$. The ω variable is related to the reciprocal turbulent time scale (frequency of vorticity fluctuations) and the k variable is the turbulence kinetic energy per unit mass. In the present work we apply the k-ω model within the pseudo-spectral framework [5,8]. The computation follows in detail the time development of the turbulent characteristics determined by the coupled non-linear transport equations accounting for a continuous generation and destruction of the turbulent energy.

For the Navier-Stokes and the heat transfer equations (1), and also the k-ω model equations, a second order implicit time discretization with iterative linearisation for the non-linear terms is used. The procedure is stable in the presented example cases. Additional two-layer ('ν_T' and 'k-ω') nested iterations are needed to obtain convergence for the non-linear terms in the k-ω equations at each time step. The electromagnetic force distribution is highly sensitive to the shape of liquid metal free surface and is recalculated at every time step. The computational procedure for the electromagnetic field is implemented with the same grid as the fluid dynamic equations, which ensures a high resolution within the surface boundary layer because of the dense grid in this region. The electromagnetic force **f** is computed by the previously tested [5] accurate integral equation based algorithm. In the AC case the time-average force in the fluid is concentrated in the skin layer and it is variable along the layer. This means that, however small the skin layer depth is, the force is always rotational and drives the fluid flow.

Induction dynamic melting simulation results

Semi-levitation (Suspension melting). Let us consider a moderate power (200 kW) magnetic semi-levitation device with a five turn coil (+ 1 turn opposite direction at top) carrying 7 kA effective current at 8 kHz frequency. Initially we start with a solid ingot at room temperature. The top part starts melting first and the liquid is pushed inwards and up by the action of the electromagnetic force (Figure 1). The electromagnetic field distribution within the melt at this stage is shown in Figure 2. The coil is moving with the melting front progressing downwards to ensure the safe electromagnetic confinement at all times during the

gradual melting. A typical simulation run follows smoothly the heating and melting. The turbulent fluid flow with the associated electromagnetic field is continuously updated until a final quasi-stationary flow field is established, and the thermal balance within the melt is achieved when the melting is completed. At the final time moment solid material is left at the very bottom, covering the water-cooled copper base hole and preventing the liquid metal from pouring into a mould below the melting device (Figure 3). When this last solid metal melts, the liquid metal flows freely downwards through the axial hole out of the magnetic confinement.

Cold crucible (Induction Scull Melting – ISM). In the ISM process the coil position is fixed behind the water cooled sectioned copper wall (see Figure 4 for the final stage). If the initial charge is of cylindrical shape, there is usually a gap at the sidewall. After the melting starts the temperature is highest in the surface film zone and the heat is slowly penetrating the rather thick cylindrical charge in the radial direction. At the following couple of seconds the gravity driven flow is directed mainly downwards, waving and filling the bottom gap. After the initial stage, when the bottom corner is filled, the largest h;lleating concentration is shifted to the bottom part of the side skin layer, which is now closer to the source coil and the segmented wall induced electric currents. Subsequently the melting front progresses slowly radially inwards. The heat conduction coefficient within the solid part is small compared to the turbulent flow region and the phase change from solid to liquid consumes significant energy. The bottom cooling takes away heat efficiently leaving the bottom gap filled. At the final stage (Fig. 4) almost all of the charge metal is liquid; only a thin mushy zone film is left at the bottom. The overall superheat is less than 50 degrees C because of the very efficient turbulent heat transport to the water-cooled walls and bottom. The electromagnetic field supports the shape with the linearly decreasing force distribution along the height, in proportion to the gravity-produced pressure at the side surface. The current and the heating are induced in the side layer, from where the intense turbulent mixing distributes the heat. The final distribution of the turbulence energy shows collection of highly turbulent fluid at the top where the turbulence from the source region at the side surface (where rotational force acts) is advected. The mushy zone damps the turbulence efficiently. No significant destruction of the turbulence occurs at the top free surface with the zero stress boundary condition. The flow and the temperature distribution changes dramatically when the electric current is switched off in preparation to pouring of the molten metal into a casting mould.

Energy efficiency. The relative importance of the heat losses at the free surface by radiation and the water-cooled crucible bottom and the walls (where liquid metal directly contacts, e.g., a cold crucible) can be estimated from the computed heat fluxes. The heat flux in general is defined as

$$Q = \oint \rho C_p \alpha_e \nabla T \cdot \mathbf{n}\, dS_n = Q_R + Q_S \,. \tag{3}$$

The heat loss from the charge by radiation Q_R is the flux integrated over the free surface (not contacting to the solid bottom and walls). The effective heat flux at the solid walls Q_S is the flux integrated over the surface contacting the solid bottom and walls. At the final thermal balance situation, when the total input Joule heating equals the summary surface heat loss, the heat loss to the water-cooled bottom and the walls Q_S is dominant in the cold crucible (see Figure 5). The heat balance saturation is not achieved for the semi-levitation device, and at the final stage, close to that shown in Figure 3, the heat losses are still in their transient stage. Therefore the semi-levitation is potentially much more energy saving technique for melting.

With the aim to estimate quantitatively the overall energetic efficiency of the melting we introduce the following efficiency parameters:

$$E_f(t) = \frac{useful\_energy}{total\_energy\_input} = \frac{Q_{Ti-Al} - Q_R - Q_S}{Q_{Ti-Al} + Q_{crucible}} \,. \qquad E_{ff} = t^{-1} \int_0^t E_f(\tau) d\tau \tag{4}$$

The efficiency is a time dependent parameter. To make it more universal in characterising the overall process we integrate it over the time from the moment when the heating starts. The integral efficiency E_{ff} is also time dependent, yet shows the integral portion of the energy used for the ingot melting. At the beginning of the process the efficiency parameter shows the electrical efficiency only since at lower temperatures the radiation and the cooling loss is not active immediately. With the growing surface temperature the efficiency starts to fall, the faster the more active is the turbulent mixing enhanced cooling. Finally, when the thermal balance is achieved, the local efficiency $E_f = 0$, and the integral efficiency E_{ff} goes asymptotically to zero (the longer we keep the metal hot at the thermal balance, the more energy is lost to ambience). The integral efficiency parameter E_{ff} gives in a single curve representation the process efficiency summary as seen in Fig. 5. When melting is reaching the stage with the average temperature entering a saturation plateau, the melting is complete in principle. The integral parameter E_{ff} shows not only the efficiency of the process, but also the time, which is useful to complete the melting. The integrated efficiency parameter (4), the average temperature, the top temperature and the total electrical power released within the melt as a function of time are presented in Figure 5.

Magnetic levitation

Magnetic levitation offers possibilities for pure experiments where the effects of the wall interactions are absent. Let us consider the full electromagnetic force resolution against the commonly used magnetic pressure approximation for the high frequency AC electromagnetic skin layer controlled flow. The time average over the AC period electromagnetic force **f** can be decomposed in two parts:

$$\mathbf{f} = (\nabla \times \mathbf{B}/\mu_0) \times \mathbf{B} = -\nabla(B^2/2\mu) + (\mathbf{B}\nabla)\mathbf{B}/\mu, \qquad (5)$$

the first part being a gradient and therefore can be incorporated in a modified pressure function p_m:

$$p_m = p + B^2/2\mu. \qquad (6)$$

In general, the second part of the expression (5) contains a potential and a rotational part. But according to the commonly used thin skin layer approximation, it is neglected when determining the free surface shape of the levitated liquid. The second part is then retained only for the fluid velocity field calculation as it contains the rotational part of the force.

In this paper we want to test in series of numerical experiments, using the highly accurate spectral numerical code, the validity of the commonly used approximation neglecting the second part of (5) when determining the free surface shape. We will call this a 'potential approximation' in difference to the full electromagnetic force approximation.

The computed example considers zero gravity conditions for the purity of the numerical experiment and a single current filament surrounding a sphere at the equatorial plane. In this case we want to compute a final stationary deformation for the initial 0.5 cm diameter liquid aluminium sphere after some transition time. The final stationary shape and the velocity field are shown in Figure 6. The left side shows the potential approximation (magnetic pressure), i.e., keeping the first term only in the RHS of (5). The final velocity field, after the transitional period, is asymptotically zero in this case. There is a contrasting difference with the full electromagnetic force retained in the right side of (5) and shown on the right side of the Figure 6. The rotational force field leads to a stationary pair of symmetric toroidal vortices and the deformation is considerably smaller in comparison to the 'magnetic pressure - potential approximation'. There is a significant difference also for the transient oscillations of the liquid metal globule. Again the amplitude for the 'magnetic pressure' approximation is significantly higher in comparison to the full volume distribution of the electromagnetic force (Figure 7).

The effect can not be attributed to the $\rho v^2/2$ term being added to the effective pressure, since the Re number in this case is very small (of the order 1). However, the oscillation frequency is strikingly similar in both cases (governed by the surface tension and the globule dimension) as can be seen from the Fourier power spectra.

Finally we demonstrate a real magnetic levitation in terrestrial conditions. The numerically computed case corresponds to the classical Okress et al. experiment [10], see Figure 8. The flow field is clearly turbulent as the maximum velocity magnitude is about 0.5 m/s for the 2.5 cm diameter liquid aluminium globule. The k-ω turbulence model is applied to simulate the time dependent transitional flow within the levitated liquid metal. The electromagnetic field created by the bottom conical coil and the top stabilising coil (Fig. 8) is penetrating deep inside the levitated metal and its distribution is non-uniform along the external boundary. The resulting interface oscillations are of different frequency for the top and the bottom part of the pear shaped axisymmetric liquid volume. The total electromagnetic force acting on the liquid volume and the position of the centre of mass are also oscillating with the shape change. The computed turbulent viscosity is time variable and adjusts to the turbulent kinetic energy creation, convection, diffusion and destruction. Special attention is paid to the boundary conditions for the turbulence characterising quantities, as the whole boundary is the free surface. Experiments with a higher AC frequency demonstrate similar behaviour as the presented cases, yet require more computational effort.

Aluminium electrolysis problem

An aluminium electrolysis cell is a part of similar cells in a very long row where each cell is connected in series to the neighbours by a complex arrangement of current carrying bus bars shown in Figure 9 for a particular case of side-to-side type cell. The electric current to an individual cell is supplied from above via massive anode bus bars made of solid aluminium, from which anode rods connect to the carbon anodes [18]. There are significant gaps between the sidewalls and the anode carbon, which are known as side channels. The side channels and the layer where the anodes are immersed are filled with a relatively poorly electrically conducting ($\sigma_2 = 2\cdot10^2$ $(\Omega\cdot m)^{-1}$) liquid electrolyte. The liquid electrolyte layer beneath the anode blocks is of a small depth (4-6 cm) if compared to its horizontal extension (2-3 x 6-15 m). The electrolyte density $\rho_2=2.1\cdot10^3$ kg/m^3 is of little difference to the liquid aluminium ($\rho_1=2.3\cdot10^3$ kg/m^3 , $\sigma_2 = 4.5\cdot10^6$ $(\Omega\cdot m)^{-1}$) collecting as the result of electrolytic reaction at the bottom liquid layer of the depth 20 – 30 cm and similar horizontal extension as the electrolyte layer. For the "shallow water" approximation the horizontal dimensions L_x and L_y are assumed to be much larger than the typical depth H, and the interface wave typical amplitude A is assumed to be small relative to the depth. The two small parameters of the problem are the nondimensional depth δ and the amplitude ε:

$$\delta = \frac{H}{L} << 1, \qquad \varepsilon = \frac{A}{H} << 1. \tag{7}$$

With the purpose to derive weakly non-linear shallow layer approximation Boussinesq equations for the wave motion we will need to estimate the terms in the full three dimensional Navier-Stokes equations of motion. Therefore nondimensional variables are introduced using the following typical scales: the width of cell L for the co-ordinates x,y; $u_0 = \sqrt{gH}$ for velocity **v**, $L/\sqrt{gH}$ for time t, $\rho_1 u_0^2$ for pressure p, IB_0/L^2 for the electromagnetic force **f** (B_0 is typical magnetic field magnitude and I – the total electric current). According to the small depth assumption a stretched nondimensional vertical co-ordinate

$$\bar{z} = z/(L\delta) \tag{8}$$

is defined, and the nondimensional interface deformation of small amplitude is represented as

$$H_0/(L\delta) = \bar{H}_0 = \varepsilon\varsigma(x,y,t). \tag{9}$$

With these definitions the nondimensional fluid flow equations: continuity, horizontal momentum and vertical momentum transport, are respectively:

$$\partial_k u_k + \delta^{-1}\partial_{\bar{z}} w = 0 \tag{10}$$

$$\partial_t u_j + u_k\partial_k u_j + \delta^{-1} w\partial_{\bar{z}} u_j = -\partial_j p + \mathrm{Re}^{-1}(\delta^{-2}\partial_{\bar{z}}\bar{\nu}_e\partial_{\bar{z}}u_j + \partial_k\bar{\nu}_e\partial_k u_j) + E f_j \tag{11}$$

$$\partial_t w + u_k\partial_k w + \delta^{-1} w\partial_{\bar{z}} w = -\delta^{-1}\partial_{\bar{z}} p + \mathrm{Re}^{-1}(\delta^{-2}\partial_{\bar{z}}\bar{\nu}_e\partial_{\bar{z}}w + \partial_k\bar{\nu}_e\partial_k w) + E f_z - \delta^{-1}, \tag{12}$$

where the summation convention is assumed over the repeating k indexes (equal to 1 or 2, respectively for x, y co-ordinates), $\bar{\nu}_e$ is the nondimensional effective turbulent viscosity, f_j are the components of electromagnetic force, and the last term in (12) represents the constant gravity. The nondimensional governing parameters are the Reynolds number and the electromagnetic interaction parameter:

$$\mathrm{Re} = Lu_0/\nu, \qquad E = \frac{IB_o/L^2}{\rho u_0^2/L} = \frac{IB_o}{L^2\rho g\delta}. \tag{13}$$

An important feature of the shallow water approximation is the depth averaging procedure defined for the problem variables in each layer [22]. The same depth averaging procedure formally can be applied to the fluid flow equations (10)-(12). When the depth averaging procedure is applied to the horizontal momentum equations (5), the equations for the horizontal circulation $\mathbf{u}_0$ plus ε-order $\hat{\mathbf{u}}_\varepsilon$ wave motion: $\hat{\mathbf{u}} = \hat{\mathbf{u}}_0 + \hat{\mathbf{u}}_\varepsilon$ for each of the fluid layers are found [19,20,22]. The appropriate boundary conditions to solve the equations are zero normal velocity and zero tangential horizontal circulation velocity components at the side walls:

$$\hat{u}_n = 0 \quad \text{and} \quad \hat{u}_{0\tau} = 0. \tag{14}$$

The horizontal velocities are intricately coupled owing to the problem non-linearity and, most importantly, by the electromagnetic field dependence on the interface ς variation. The depth average momentum and continuity equations for the two fluid layers can be combined in one non-linear wave equation for the interface:

$$\left\langle\frac{\rho}{h}\right\rangle\partial_{tt}\varsigma - \frac{1}{3}\langle\rho h\rangle\partial_{ttjj}\varsigma + \left\langle\frac{\mu\rho}{h}\right\rangle\partial_t\varsigma + \langle\rho g\rangle\partial_{jj}\varsigma = \langle\partial_j F_j\rangle - \left\langle\frac{\rho}{h}\partial_{tj}(\varsigma u_{jo}) + \rho\partial_j(u_{ko}\partial_k u_{jo}) + \frac{\mu\rho}{h}\partial_j(\varsigma u_{jo})\right\rangle \tag{15}$$

where $\langle F\rangle = F_1 - F_2$ denotes a difference of variables in the two layers, F_j – the electromagnetic force components (effectively including the vertical force), ρ_i – density, μ_i – friction coefficient [21], h_i – undisturbed depth for each layer (h_1 =0.25, h_2 =0.05 m in the following computed examples).

We demonstrate the importance of the wave non-linearity with the example of non-linear gravity wave at the interface of electrolysis cell in the absence of the electromagnetic force. If starting with (1,0) natural gravity wave perturbation, the difference between the linear and non-linear sloshing wave development is demonstrated in Fig.10. The final non-linear wave spatial profile is very close to the analytical solution by Tadjbakhsh & Keller (see details in [19]). With the full electromagnetic interaction included, which is computed for a specific 122 kA industrial cell including the full 3-dimensional bus-bar representation (Fig.9) and the steel ferromagnetic construction elements [23], the same initial perturbation grows over a large time period of 1000 s even with the turbulent friction included (Fig 11a). The initial perturbation is completely damped and the magnetically shifted frequency [22] is dominant finally (Fig 11b). The turbulent horizontal flow (Fig. 12) is non-linearly coupled to the interface waves and to the full electromagnetic field variation.

Conclusion. The presented model calculations show a reasonable correspondence to the variety of dynamic industrial applications and permit to analyse flow patterns, free surface stability and to estimate the energy efficiency of the processes. The modelling procedure can be extended to other generally unsteady flows with the moving melting fronts and free surfaces. A detailed time history and the clear physical insight to the driving forces and the sequence of events are available from the simulations.

References

1. E. Taberlet and Y. Fautrelle: J. Fluid Mech., 159(1985), 409.
2. E. Baake, A. Muhlbauer, A. Jakowitsch and W. Andree: Metall. Mater.Trans. 26B(1995), 529.
3. H. Fukumoto, Y. Hosokawa, K. Ayata and M. Morishita: MHD in Process Metallurgy, TMS (1991), 21.
4. R. Kageyama and J.W. Evans: Metall. Materials Trans., 29B(1998), 919.
5. A.Bojarevics, V.Bojarevics, J.Gelfgat and K.Pericleous: Magnetohydrodynamics, 1999, 35, N3, 258.
6. R. Moreau: *Magnetohydrodynamics*, Kluwer, Dordrecht/ Boston / London (1990).
7. D.C.Wilcox: *Turbulence Modelling for CFD*, 2nd ed., DCW Industries, California (1998).
8. V. Bojarevics, K. Pericleous and M. Cross: Metall. Materials Trans. B, 2000, vol. 31B, 179.
9. V.Bojarevics, J.Freibergs, E.Shilova, E.Shcherbinin. Electrically Induced Vortical Flows. "Kluwer Academic Publishers", Dordrecht / Boston / London (1989), 392 p.
10. 1. E. Okress, D. Wroughton, G. Comenetz, P. Brace and J. Kelly: *J. Appl. Phys.*, 1952, vol. 23 (5), pp. 545-52.
11. A. Gagnoud and J.P. Brancher: *IEEE Trans. Magn.*, 1985, vol. 21 (6), pp. 2424-27.
12. C.H. Winstead, P.C. Gazzerro and J.F. Hoburg: *Metall. Materials Trans. B*, 1998, vol. 29B, pp. 275-81.
13. J. Szekely and E. Schwartz: *Int. Symp. Electromagn. Process. Mater.*, ISIJ, 1994, Nagoya, pp. 9-14.
14. S.P. Song and B.Q. Li: *Transactions ASME, J. Heat Transfer*, 1998, vol. 120, pp. 492-504
15. A.J. Mestel: *J. Fluid Mech.*, 1982, vol. 117, pp. 27-43.
16. A.D. Sneyd and H.K. Moffatt: *J. Fluid Mech.*, 1982, vol. 117, pp. 45-70.
17. P. Sryanarayana and Y. Bayazitoglu: Phys. Fluids A, 1991, vol. 3, N 5, pp. 967-977.
18. K. Grjotheim and H. Kvande (Editors): *Introduction to aluminium electrolysis.* Aluminium-Verlag, Dusseldorf. 1993.
19. V. Bojarevics: *Progr. Fluid Flow Res.: Turbulence and Applied MHD,* eds. H.Branover and Y.Unger, AIAA, 1998, Chapter 58, pp.833-848.
20. O. Zikanov, A. Thess, P.A. Davidson and D.P. Ziegler: *Proc. 3rd Int. Symp. Electromagnetic Processing Materials,* Nagoya, 2000, Iron and Steel Institute Japan, pp. 109-114.
21. R. Moreau and J.W. Ewans: *Journal of Electrochemical Society*, Vol. 131, 1984, No 10, pp.2251-2259.
22. V. Bojarevics and M.V. Romerio: *Eur. J. Mech., B/Fluids*, Vol.13, No 1, 1994, pp.33-56.
23. J. Freibergs: *Proc. Int. Colloq. 'Modelling Material Processing' Riga, Latvian University*, 1999, pp.86-91.

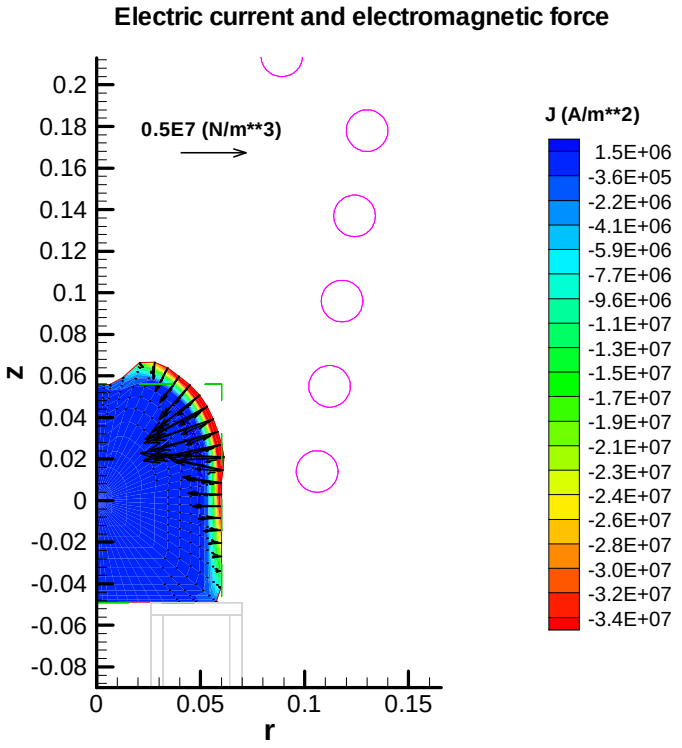

Figure 1. The electromagnetic field distribution within the melt at the initial melting stage in the semi-levitation device.

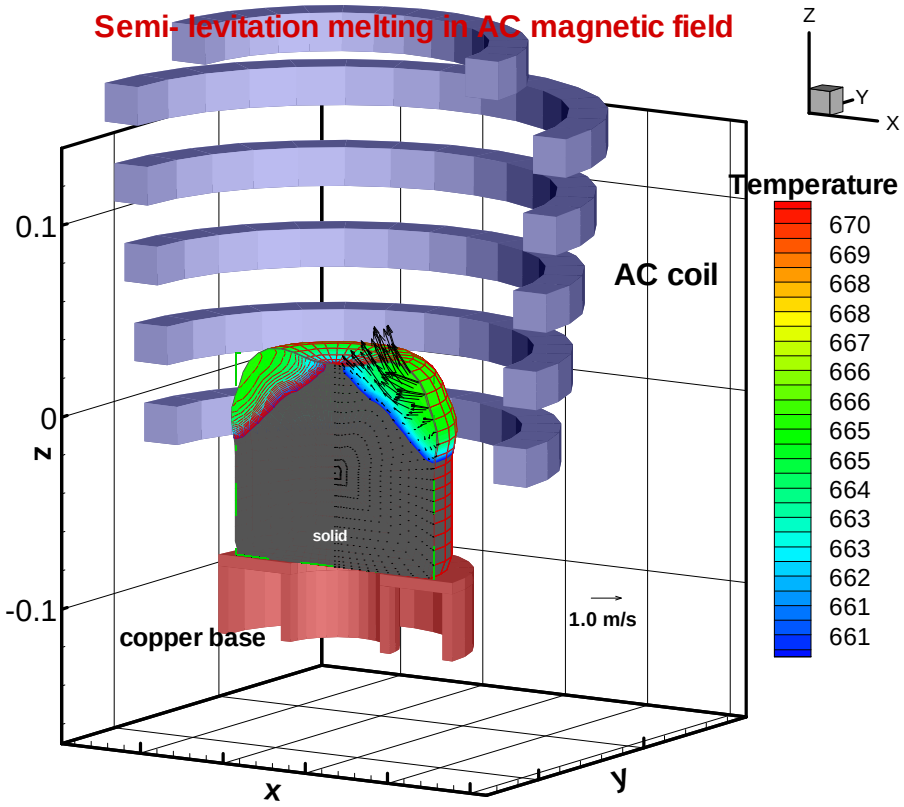

Figure 2. The initial stage of melting aluminium in the semi-levitation device.

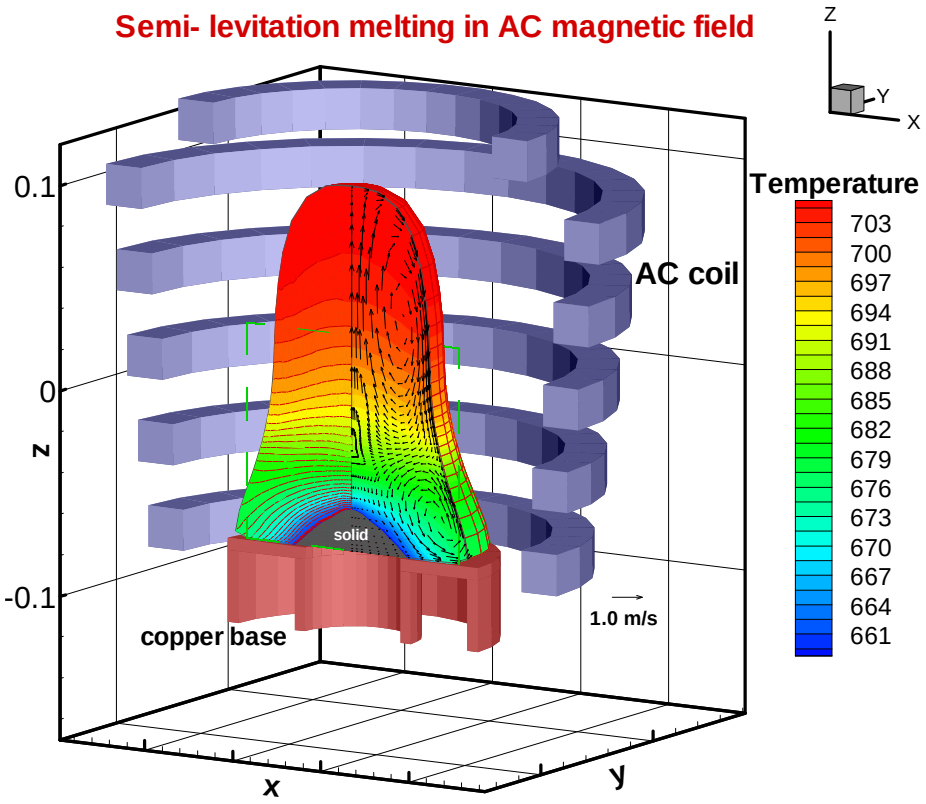

Figure 3. Melting at the final crucial stage when confinement and stability must be achieved.

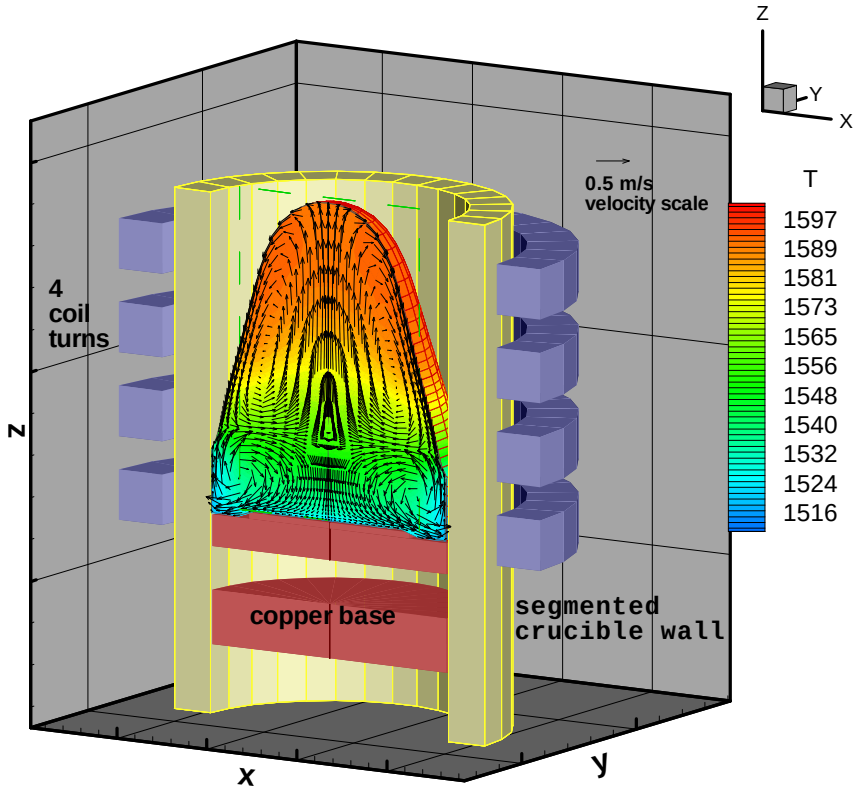

Figure 4. Cold crucible melting of Ti-Al alloy: quasi-stationary stage when melting is completed.

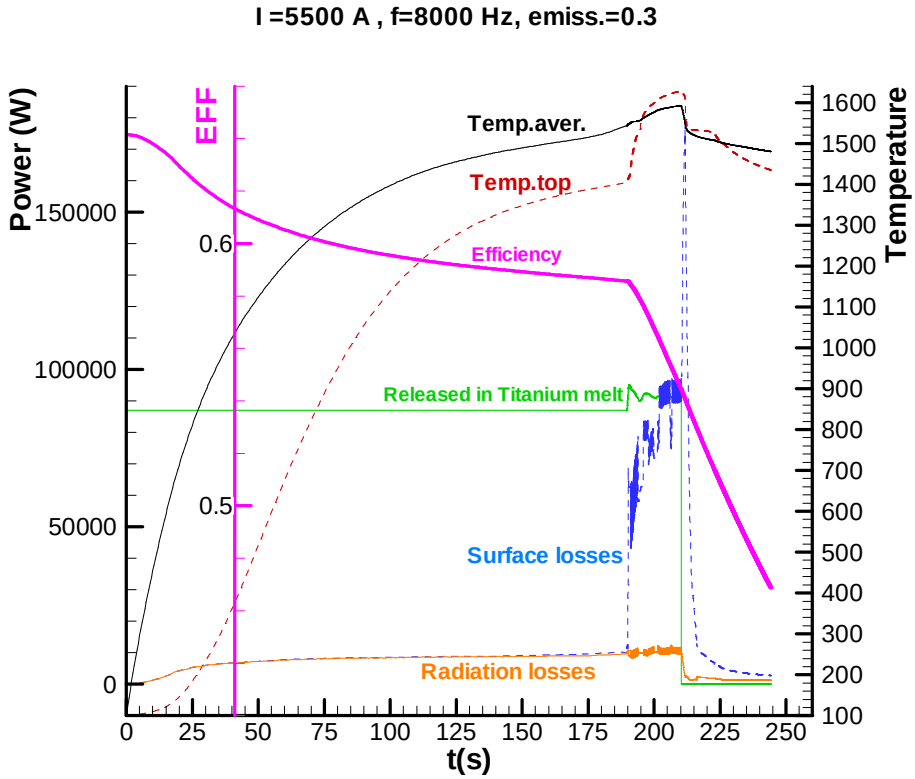

Figure 5. Power, temperature and the efficiency time history during melting. See text for detailed discussion.

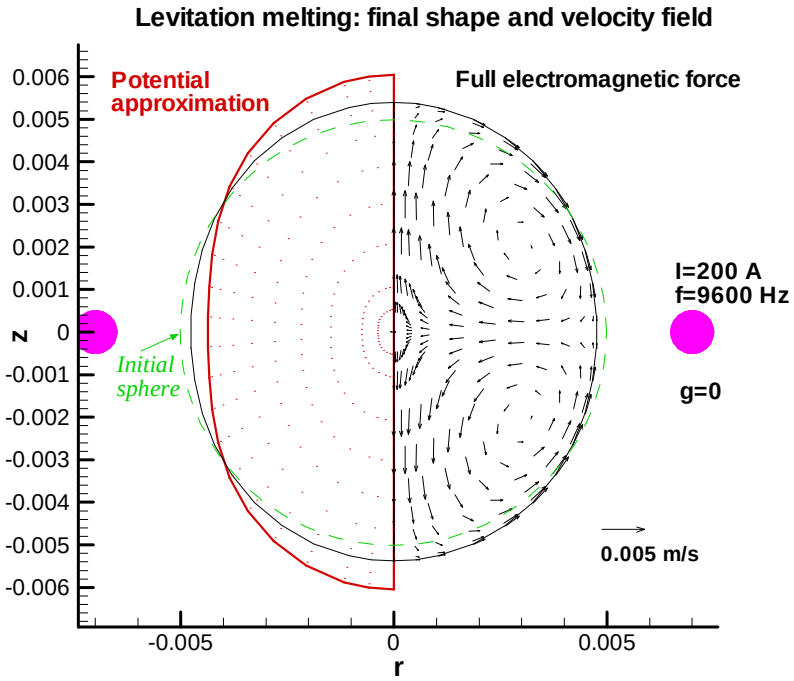

Figure 6. The zero gravity and single current loop numerical experiment. Comparison of the free surface deformation and the velocity field at the final stationary stage for the 'potential approximation, magnetic pressure' and the full electromagnetic force cases.

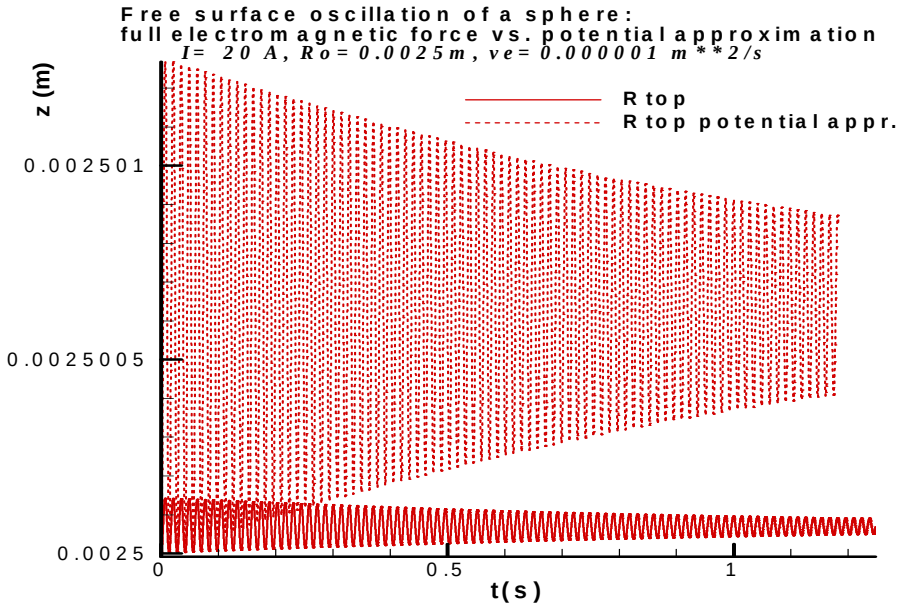

Figure 7. The decaying free surface oscillations for the laminar viscosity fluid sphere at zero gravity after switching-on the current in the current loop: 'potential approximation, magnetic pressure' and the full electromagnetic force cases.

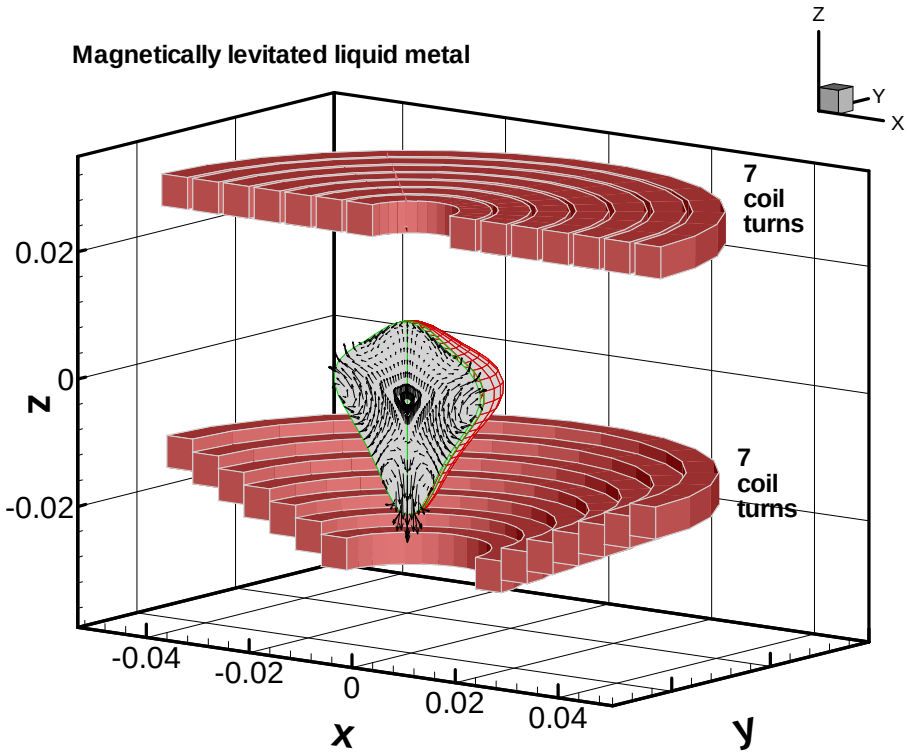

Figure 8. Numerical simulation of the free surface and turbulent flow in the Okress et al. [10] experimental configuration.

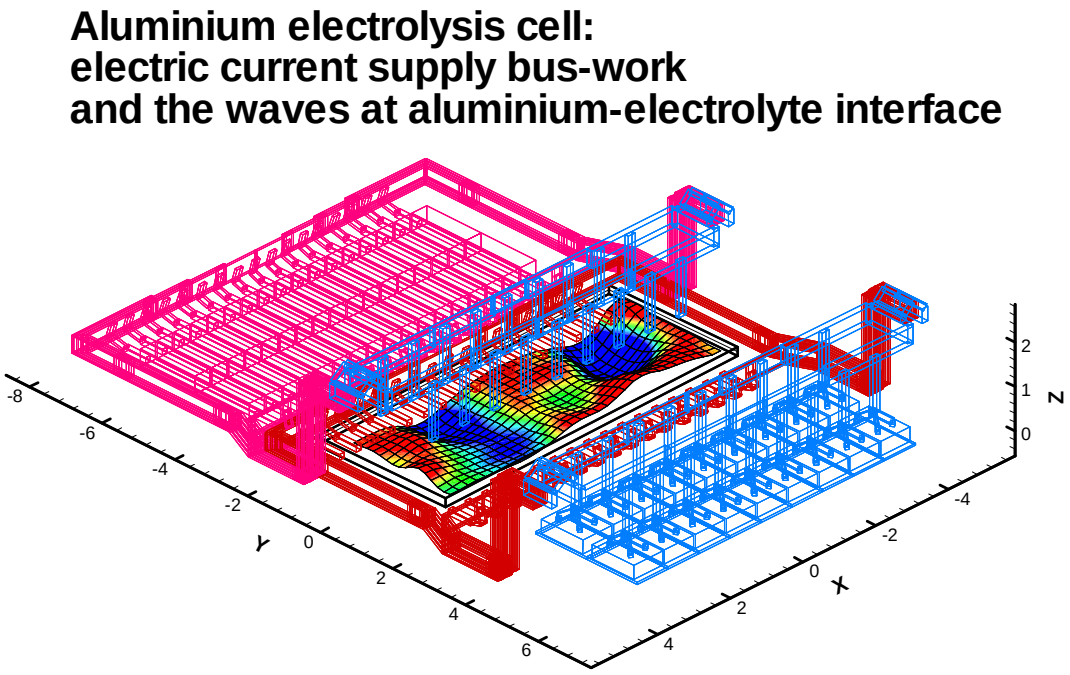

Figure 9. The bus bar configuration for a test cell in series of similar cells (waves are shown in the test cell and the bus bars are extended to the two neighbour cells).

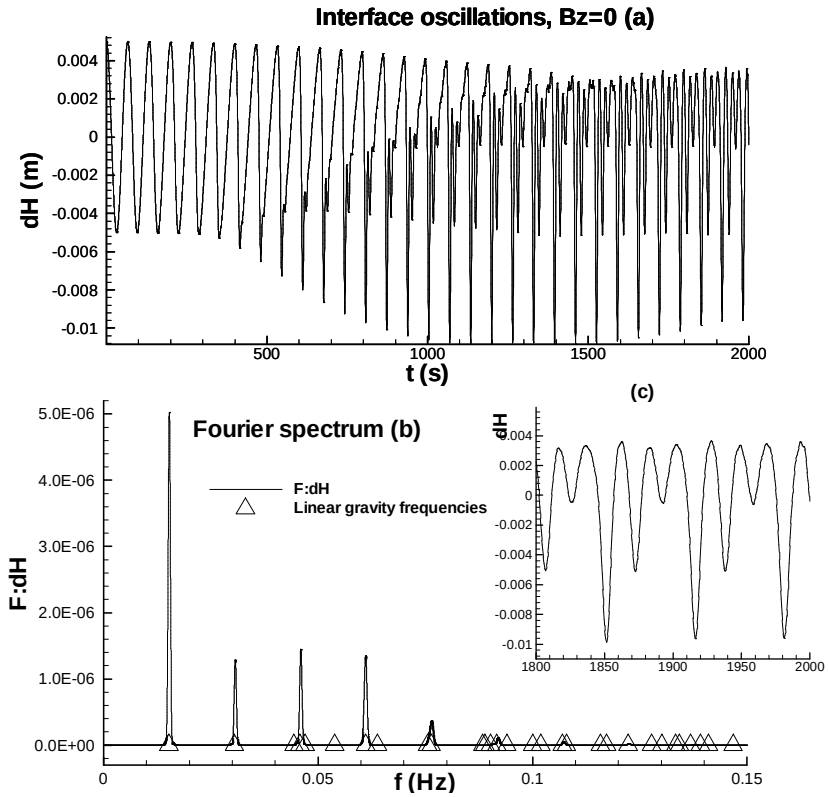

Figure 10. Non-linear wave evolution from the (1,0) natural gravity wave initial perturbation.

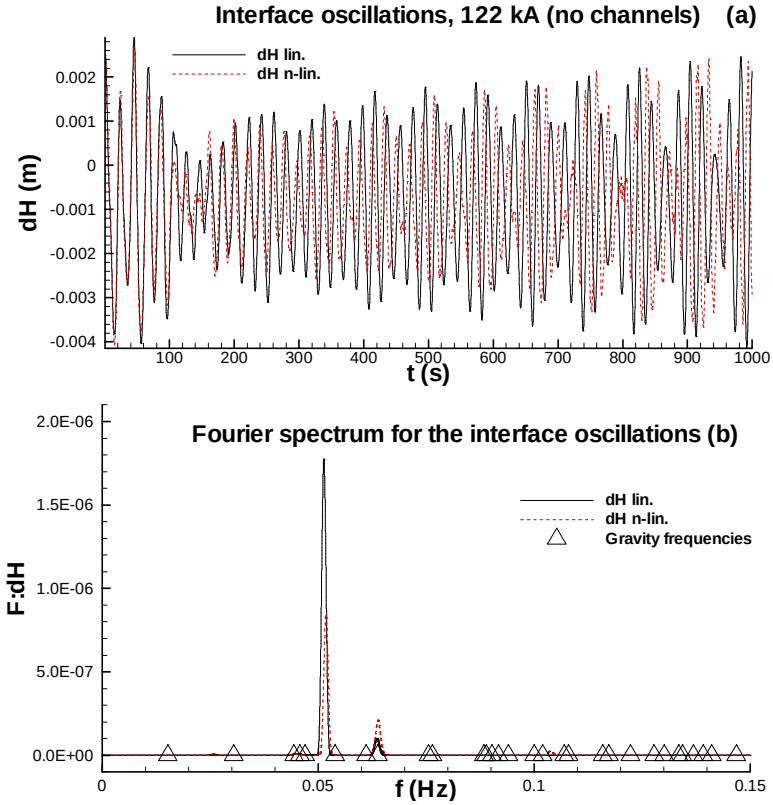

Figure 11. Comparison of the linear and non-linear wave approximations in the case of full magnetic field for the 122 kA commercial cell. The time steps are 0.25s in both cases.

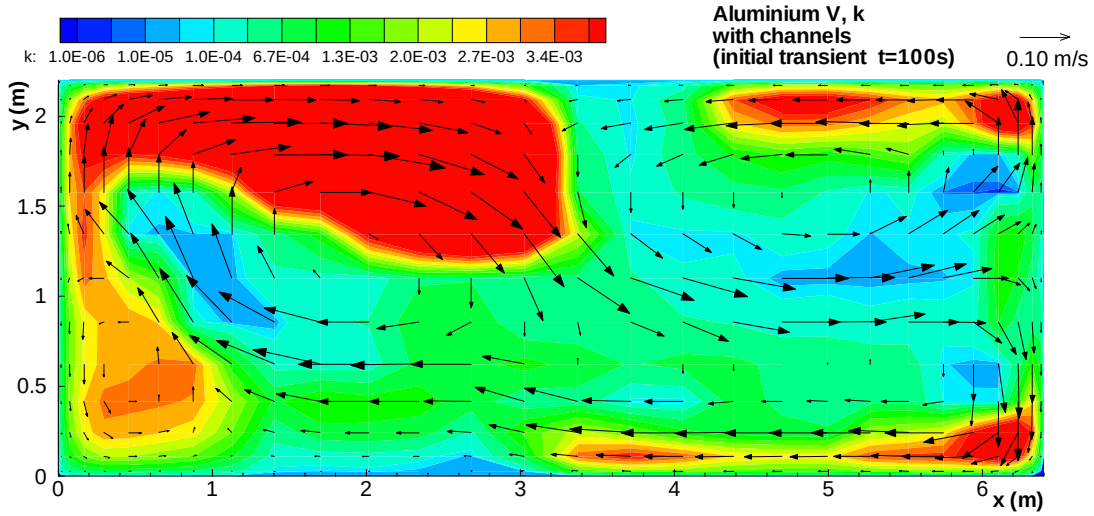

Figure 12. Velocity field and the turbulence kinetic energy distribution in the liquid aluminium layer of the 122 kA commercial cell.